APL Photonics

Photonic glass based structural color

Cite as: APL Photonics **5**, 060901 (2020); https://doi.org/10.1063/5.0006203
Submitted: 28 February 2020 . Accepted: 24 May 2020 . Published Online: 08 June 2020

Guoliang Shang, Manfred Eich, and Alexander Petrov

Photonic glass based structural color

Cite as: APL Photon. 5, 060901 (2020); doi: 10.1063/5.0006203
Submitted: 28 February 2020 • Accepted: 24 May 2020 •
Published Online: 8 June 2020

Guoliang Shang,[1,a)] Manfred Eich,[1,2] and Alexander Petrov[1,3]

AFFILIATIONS

[1] Institute of Optical and Electronic Materials, Hamburg University of Technology, Eissendorfer Strasse 38, 21073 Hamburg, Germany
[2] Institute of Materials Research, Helmholtz-Zentrum Geesthacht, Max-Planck-Strasse 1, Geesthacht, D-21502, Germany
[3] ITMO University, 49 Kronverkskii Ave., 197101 St. Petersburg, Russia

[a)] **Author to whom correspondence should be addressed:** guoliang.shang@tuhh.de

ABSTRACT

Structural coloration, which is based on spectrally selective scattering from optical structures, has recently attracted wide attention as a replacement of pigment colors based on the selective light absorption in chemical structures. Structural colors can be produced from transparent non-toxic materials and provide high stability under solar radiation. To provide angle independent non-iridescent colors, the structure should combine spectral selectivity with an isotropic response. Photonic glass (PhG), a disordered arrangement of monodisperse spheres, is a versatile structure to achieve that, which provides isotropic spectral selectivity via short-range order and Mie resonances. However, conventional PhGs show low color purity that hinders their future application. The interplay of single-particle scattering, short-range order, broadband absorption, and Fresnel reflection is a route to improve the color. In this perspective, we review the field of PhG based structural colors and discuss the physical mechanism behind the color generation by several established theories. We point out the current challenges in the theory and possible directions to improve color purity.

I. INTRODUCTION

A. Structural color

Isaac Newton showed that solar radiation can be split into different color components with transparent materials.[1,2] Based on this finding, people insistently dug into the field of the spectrally selective light scattering following Lord Rayleigh and Gustav Mie.[3] However, as the centuries passed, absorption-based pigment colors are still everywhere. They are often based on toxic chemical substances and often degrade under ultraviolet (UV) radiation.[4] Due to exposure to solar radiation, outdoor colors need to be repainted every few years to repair the fading.[4] Thousands of ancient paints and arts need to be carefully preserved under special lighting conditions to prevent an unrecoverable loss.[5,6] These are still key tasks for optical and material researchers in the near future.

Colors are generally generated by two mechanisms: selective absorption or selective scattering [Fig. 1(a)]. The selective absorption color, called pigment here, derives its colors from light absorption by electron transitions and hence leaves the unabsorbed colors reflected into human eyes.[4,7,8] Since the light absorption is dependent on the defined chemical structure, pigment colors are typically bound to particular materials, some of which are toxic and can be harmful in production, application, or disposal.[4,7,9–11] Some of the pigments can be easily altered by sun radiation or high temperature during service, initiating the need for alternatives.[4–6] Different from that, structural colors[12–19] are based on light scattering and reflection from the structure, which depends only on the refractive index distribution, and thus can be produced from environmentally friendly transparent materials and bears the potential of high solar radiation and temperature stability.[20] Iridescent structural colors based on periodical structures with a periodicity in the order of visible light wavelength, known as photonic crystals (PhCs),[13,15,21–24] show bright color impressions but different colors at different viewing and illumination angles. To substitute pigments, non-iridescent structural colors are required. To achieve an angle-independent color, the current concepts are based on disordered microstructures mimicking biological structures,[25–29] photonic glass [PhG; Figs. 1(b) and 1(c)],[27,30–35] polycrystal PhCs,[26,36] and superballs with a PhC as the radial coating.[37–39] There are also angle-independent structural color concepts based on thin-film geometries,[40–43] but they require

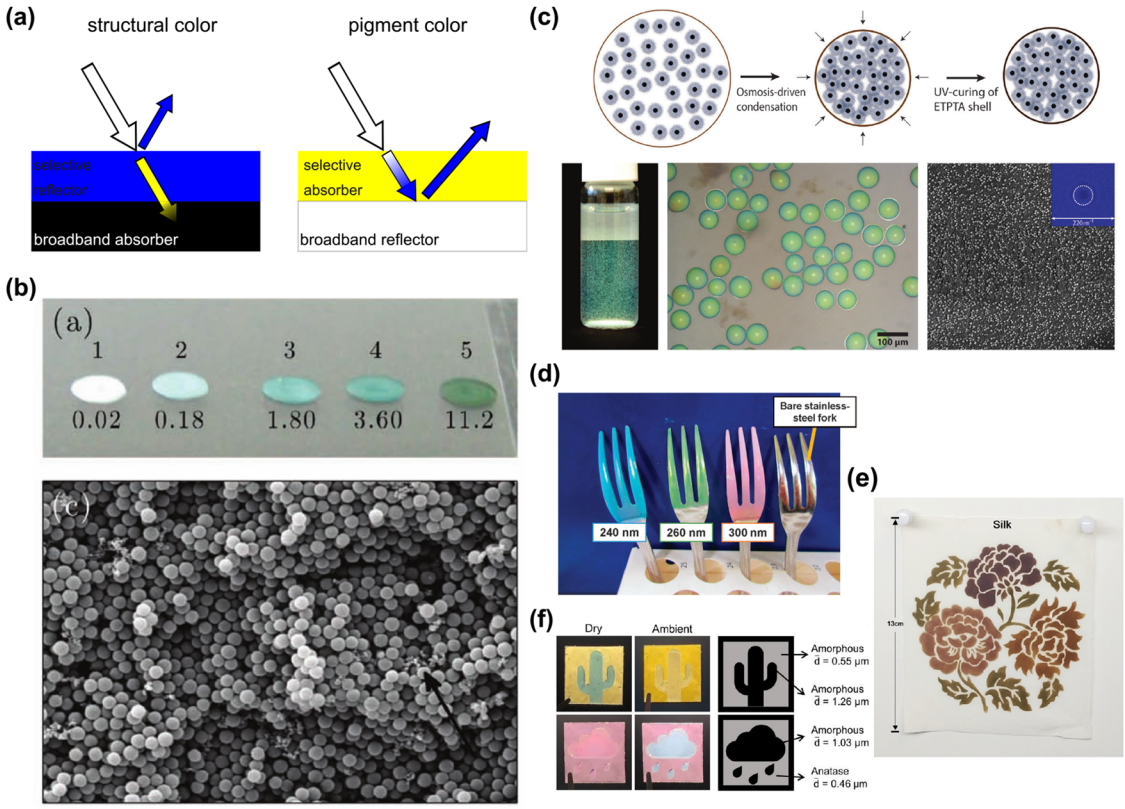

FIG. 1. (a) Colors via selective reflection or selective absorption. (b) Structural color impressions of PhGs out of a mixture of 226 nm and 265 nm spherical polystyrene (PS) particles. The carbon black concentration varies from 0.02 wt. % to 11.2 wt. % from left to right. The SEM image of the disordered arrangement of PS particles (sample 3). Reprinted with permission from Forster *et al.*, Adv. Mater. **22**, 2939 (2010). Copyright 2010 Wiley-VCH. (c) The fabrication process of a photonic capsule with the PhG out of core–shell particles, the photograph and an optical micrograph of the capsules in water, the cross section SEM image, and the inset showing the corresponding 2D Fourier transform. Reprinted with permission from Park *et al.*, Angew. Chem., Int. Ed. **53**, 2899 (2014). Copyright 2014 Wiley-VCH. The structural colors out of PhG can be used as paint coatings on different surfaces as (d) coated stainless steel made forks showing different colors with different sizes of particles or (e) silk. Reprinted with permission from Katagiri *et al.*, NPG Asia Mater. **9**, e355 (2017). Copyright 2017 Author(s), licensed under a Creative Commons Attribution 4.0 License. Meng *et al.*, ACS Appl. Mater. Interfaces **11**, 13022 (2019). Copyright 2019 American Chemical Society. (f) The PhG structural color can be used as a label-free sensor to monitor the humidity. Reprinted with permission from Mohd-Noor *et al.*, J. Mater. Chem. A **7**, 10561 (2019). Copyright 2019 Royal Society of Chemistry.

flat substrates and a special deposition technology that can hardly be applied to arbitrary substrates. Particularly interesting is also the combination of pigments and structural scattering to obtain new or better colors.[44,45]

B. Photonic glass

The term "photonic glass" appeared as an analog to "photonic crystal."[30,31] PhG is a disordered arrangement of monodisperse spherical particles with short-range order only, which appears due to physical contact between particles.[30,31,46] A hard-sphere random arrangement system can be considered as a frozen liquid structure.[46,47] It should be mentioned that depending on the packing algorithm or experimental procedure, different random arrangements can be obtained, differentiating in terms of randomness and packing density.[46,48]

PhG has attracted a lot of attention in the field of non-iridescent structural colors due to the straightforward production procedure and applicability as a coating on arbitrary surfaces [Figs. 1(d)–1(f)].[49,50] Due to the intrinsic isotropic arrangement of the particles, the spectral characteristics under diffuse illumination are independent of the observation angle. A PhG from homogeneous spherical dielectric particles was used for the non-iridescent blue structural color[35,44,51,52] with color properties similar to what is observed in nature.[53] Since the wavelength range of the strong backscattering is related to the interparticle distance and the average refractive index, other colors were addressed by varying the size and/or the dielectric strength of the particles.[25,27,32,35,52,54–60] Furthermore, core–shell particles,[34,39,61,62] hollow particles,[54,61,63] and broadband absorbers[32,35,49,58,64–69] were added into PhGs to improve the color purity. Several examples show the application perspectives of the PhG structural color as color paints [Figs. 1(d)–1(f)].[49,50,52,70] Since the color impression will change with the interparticle distance,[57,71] PhG structural colors can also be used as a stress response smart window,[72] electric field-induced color variation,[73–76] and a humidity sensor [Fig. 1(f)].[77]

However, the presented PhG based structural colors still show quite a low color purity, which hinders future applications.[32,62,78] In general, the non-absorbing PhG layer reflects light as a high-pass filter (high frequencies and small wavelengths are reflected).[34,62,79] Thus, it is relatively easy to obtain a blue color, where the reflection in the UV range, due to its invisibility, does not affect the color impression. To obtain other colors, the reflection of shorter visible wavelengths must be suppressed to retain a pure color impression.[32,49,62,80] Also, the transition from weak reflection to strong reflection should be sharp to improve color purity.[34] Therefore, understanding the scattering properties of a PhG structure is crucial for the improvement of PhG-based structural colors. In the recent few years, the first-order scattering approximation,[33,34,51,79,81] Mie scattering/resonances,[31,39,71,82–84] the diffusion theory,[85–89] and combinations of them were introduced to describe the mechanism of color generation from PhGs. In this perspective, we will discuss the existing theories and present approaches to improve color purity and draw outlook for further improvements.

II. THEORY

A. Color definition

There are only three kinds of cone cells (color receptors) sensing the light in human eyes with a sensitive wavelength in blue, green, and red color, respectively. These cells translate the received light signal [e.g., blue, green, or red light in Fig. 2(a) reflected from objectives Figs. 2(b) and 2(c)] into color impressions in the human brain. According to that, a color space maps a range of discernible colors to an objective description of color sensations registered in the human eye, as tristimulus values (X, Y, Z) related to the signal levels coming from each cone cell and depending on the reflected optical power, to describe the color impressions,[2,90]

$$\begin{cases} X = \frac{1}{N}\int_\lambda R(\lambda)I(\lambda)\bar{x}(\lambda)d\lambda, \\ Y = \frac{1}{N}\int_\lambda R(\lambda)I(\lambda)\bar{y}(\lambda)d\lambda, \\ Z = \frac{1}{N}\int_\lambda R(\lambda)I(\lambda)\bar{z}(\lambda)d\lambda, \end{cases} \tag{1}$$

where $\bar{x}(\lambda)$, $\bar{y}(\lambda)$, and $\bar{z}(\lambda)$ are the color matching functions (colored curves in Fig. 2(a), $N = \int_\lambda I(\lambda)\bar{y}(\lambda)d\lambda$ is a normalization factor that ensures Y represents the reflectance strength, λ is the light wavelength (measured in nanometers), and the limits of the integral are $\lambda \in [380, 780]$. For the comparison of an arbitrary illumination source, the spectral power distribution of the illuminant $I(\lambda)$ can be treated as 1. $R(\lambda)$ is the reflection spectrum of the object. Then, the chromaticity of a color is specified by the two derived parameters x and y, two of the three normalized values being functions of all three tristimulus values,[2]

$$\begin{cases} x = \frac{X}{X+Y+Z}, \\ y = \frac{Y}{X+Y+Z}, \\ z = \frac{Z}{X+Y+Z} = 1 - x - y. \end{cases} \tag{2}$$

The chromaticity diagram such as the International Commission on Illumination (CIE) 1931 color space [Fig. 2(d)] is commonly used. In such a diagram, a fully saturated, pure color originating from a single wavelength can be found on the outer perimeter. A completely unsaturated color such as gray or white is located in the so-called white point at the center of the diagram (1/3, 1/3). A certain complete subset of colors is called the gamut. Hue stands for the visual perception of color, which can be defined on the outer perimeter of the color diagram. Red, green, yellow, and blue are known as unique hues. These spectra illustrations in Figs. 2(b) and 2(c) are deliberately chosen. For the concept of the blue and red colors out of PhG structures, the reflection transition edge is the only

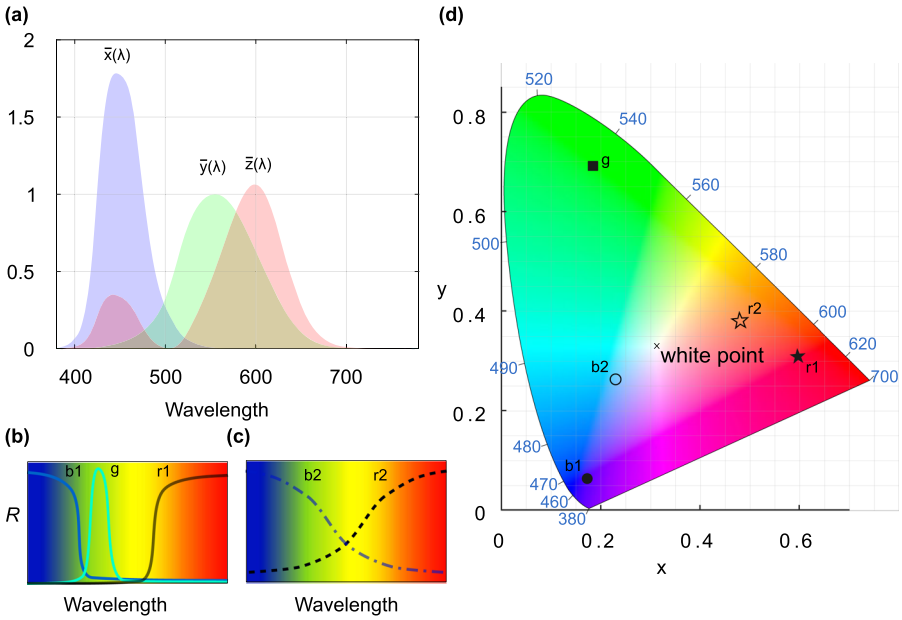

FIG. 2. (a) Color matching functions of human eyes. (b) Example reflection spectra for blue (b1), green (g), and red (r1) colors and (c) blue (b2) and red (r2) spectra with low spectral selectivity, namely, the smooth transition from weak reflection to the strong reflection region. (d) Color impressions of the curves in (b) and (c) can be calculated based on the color matching functions and with points shown in the CIE diagram. In this case, the spectral power distribution of the illuminant $I(\lambda)$ was treated as 1. The diagram further shows the white point and the positions of the pure colors on the perimeter indicated by the corresponding wavelengths in nanometer.

required feature because the light with a wavelength shorter than blue or larger than red is invisible to the human eye and will not influence the color purities. However, to achieve a high-purity color positioned in between the spectral limits of human vision, such as a green color, a peak shaped spectrum is mandatory [Fig. 2(b)]. For the non-iridescent structural colors obtained with PhGs, the color position is normally close to the white point due to the intrinsic poor spectral selectivity [Fig. 2(c)], as will be described below. Therefore, to increase spectral selectivity (namely, sharp reflection transition weak reflection to the strong reflection region) and thus color purity is the main goal of the research of structural color based on PhGs [Figs. 2(b) and 2(d)].

B. Photonic glass structure

PhG is a densely packed disordered arrangement of monodisperse particles.[30,31,46,48,91] It can be split into a disordered lattice, represented by the spheres' center points, and spherical particles as motifs. The scatterer's structure can thus be interpreted as the convolution of the lattice with the motif in the real space. In reciprocal space, the average Fourier transform (FT) of the permittivity per particle is then a multiplication of the structure factor ($\mathcal{S}$), the square of the FT of the lattice per lattice point, the form factor ($\mathcal{P}$), and the square of the FT of the motif. For the same motif, the PhG can be packed with a different packing density, which is the volume fraction occupied by the particles. The packing density of 64% is the estimated maximum value for 3D monodisperse disordered assemblies.[31,48,92] This limit can be better defined in terms of a maximally random jammed state, a state where a single particle cannot be moved freely.[48] Due to the isotropy of the short-range order in the spatial average, the structure factor is spherically symmetric and shows maxima for wavevectors corresponding to the inverse interparticle distance. The sharpness of the maxima is connected to the packing density with a maximal sharpness for the maximal packing density.[34,85,93] The approximate function of the radial distribution of $\mathcal{S}$ can be derived from solving the Ornstein–Zernike integral equation by choosing the hard-sphere Percus–Yevick approximation.[34,93,94] The Percus–Yevick approximation is a simple and accurate way to calculate the structure factor, even applicable for high packing density and polydispersities in the short k region, including the first peak of the structure factor.[95,96] The polydispersity will broaden and decrease the amplitude of the first-peak in the structure factor.[95] The self-assembling technique is a feasible way to produce such structures. To prevent the formation of an ordered structure of the colloidal suspension, the particle polydispersity, mobility, surface tension, viscosity, the volatility of the solvent, and the ionic strength of the dispersion are usually adjusted.[86,97–100]

C. Theory of scattering from photonic glass

Light scattering at a PhG structure is a complex phenomenon [Fig. 3(a)]. The particles themselves have spectral and directional scatterings due to internal Mie resonances.[3,101] Scattering of a single particle can be already quite complex due to the interplay of excited magnetic and electric multipoles in the particle.[3,102] At the same time, touching particles in the PhG lead to a modification of Mie resonances.[82] Besides, the short-range order with a periodicity comparable to the half-wavelength itself can lead to selective scattering of light even without Mie resonances.[33,81] The single scattering is a good approximation only for sufficiently thin layers (the photon mean free path is less than thickness), and thus, a photon can only experience a single scattering event before it escapes the structure. Moreover, the multiple scattering of light in the PhG can lead to a diffusive light propagation[85–89] and the geometry and the average refractive index of the PhG sample (layer or spherical agglomerate) can also introduce additional reflections at the interfaces between the PhG and the environment.[62,79,80] From the previous studies, several approximations were introduced to describe and explain the light-scattering and reflection properties of PhGs such as the first-order Born approximation, Mie scattering, and diffusion theories, which we now present and discuss.

It should be mentioned that at high refractive index contrast, strong coupling between particles can be obtained. Brute force simulation can be used then to study light propagation in such media, including the effects of light localization.[103] These effects are not considered in this review.

1. First-order Born approximation

The light-scattering properties of a structure with a small permittivity contrast $\Delta\varepsilon(\vec{r})$ with respect to the background can be estimated from the first-order Born approximation.[1,33,34,51,61,79,81,89,104] The total electric field can be expanded in Taylor series with respect to the perturbation $\Delta\hat{\varepsilon}$. For a small value $\Delta\hat{\varepsilon}$, the total field can be reasonably well approximated by the first-order term. The excess polarization induced by the incident wave as a source gives rise to the scattered waves.

The Ewald sphere construction derived from the first-order Born approximation geometrically predicts the wavelength dependence and the directions of the scattered light [Figs. 3(b) and 3(c)] by the overlap of the Ewald sphere and the spatial FT of the permittivity distribution $\Delta\varepsilon(\vec{r})$. The Ewald sphere in reciprocal space has the radius of the incident wave number and is shifted from the center of reciprocal space by negative of the incident wavevector $-\vec{k}_{in}$. It can visualize the Bragg conditions fulfilled for the gratings in the structure [Fig. 3(b)]. The FT of the PhG is represented by a spherical shell in reciprocal space, which corresponds to the first peak of the structure factor in Fig. 3(d). It shows the same periodicity along all directions due to the isotropic nature of the PhG. For the long-wavelength light (small wavenumber), there is no light scattering as no overlap between the Ewald sphere and FT of $\Delta\varepsilon(\vec{r})$ occurs [Fig. 3(c)]. Once the wavelength is short enough such that the respective growing wavenumber produces an Ewald sphere that touches the FT of the permittivity distribution, scattering sets in primarily backward. When the overlap of the Ewald sphere with the FT of $\Delta\varepsilon(\vec{r})$ increases, the scattering strength will gradually increase, thus resulting in an increase in reflectivity as the wavelengths become shorter. Scattering angles increase and reflectivity eventually saturates [Fig. 3(c)]. Due to the spherical symmetry, the overlap between the Ewald sphere and the FT for a specific wavelength will be identical for different incident angles yielding a non-iridescent reflection behavior. The permittivity of the PhG structure $\Delta\varepsilon(\vec{r})$ can be seen as the convolution of the disordered lattice function $l(\vec{r})$ with the motif function $m(\vec{r})$, where $l(\vec{r})$ represents the distribution of the spheres' center points in space and $m(\vec{r})$ represents the distribution of the permittivity difference in the motif. In

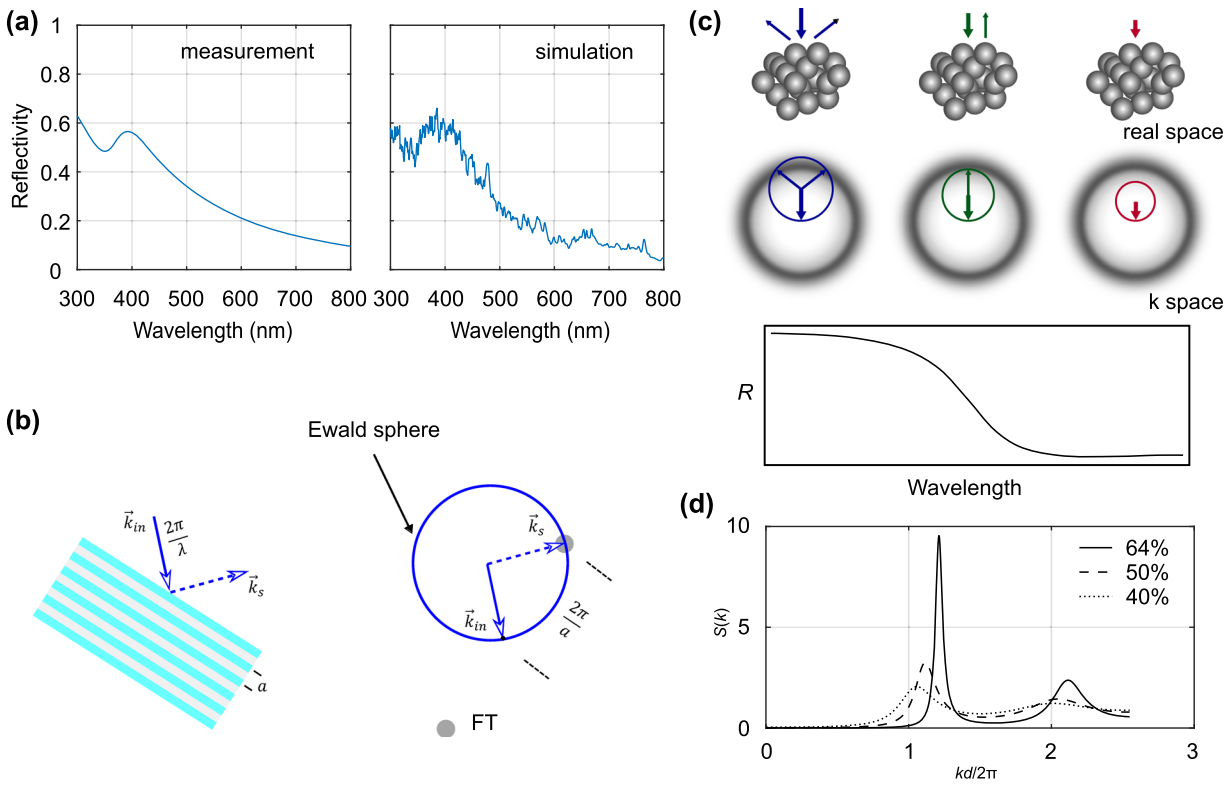

FIG. 3. (a) Measured diffuse reflection spectrum from a PhG film from the 172 ± 6 nm PS particle and a film thickness of 5.3 μm and the simulated spectrum from a volume of 1.8 × 1.8 × 5.3 μm^3 PhG-film with the particle refractive index n_{PS} of 1.6, size of 172 nm, packing density of 64%, and in the background material n_b of 1. (b) Ewald sphere (blue circle) construction illustrates the Bragg condition reflection of a Bragg grating (lattice constant a). The incident light with a wavelength of λ ($k_{in} = \frac{2\pi n_b}{\lambda}$) and direction $\vec{k}_{in}$ can be scattered only when the Ewald sphere crosses the FT function of the Bragg grating permittivity distribution (two peaks at a distance of $\frac{2\pi}{a}$ to the reciprocal space center). The scattering direction is defined by $\vec{k}_s$. (c) The schematic real and reciprocal space representation of the PhG structure, including Ewald sphere construction,[79] and the corresponding illustration of the half-space reflection spectrum. The thick colored arrows stand for the incident and the thin colored arrows stand for the scattered waves, with the corresponding Ewald spheres illustrated by colored circles. (d) Structure factor function of the PhG with different packing densities.

reciprocal space, the FT of the whole structure is the multiplication of the lattice FT $\mathcal{F}_l(\vec{k})$ and the motif FT $\mathcal{F}_m(\vec{k})$,[34]

$$\mathcal{F}\{\Delta\varepsilon(\vec{r})\} = \mathcal{F}\{l(\vec{r}) \otimes m(\vec{r})\} = \mathcal{F}_l(\vec{k}) \cdot \mathcal{F}_m(\vec{k}). \tag{3}$$

Thus, the average intensity of scattered light per motif in the lattice is proportional to the product of the structure factor $\mathcal{S}$ [Fig. 3(d)] and the form factor $\mathcal{P}$, where the latter is the square of the motif FT normalized by the volume of the motif (V) and can be written as $\mathcal{P} = |\mathcal{F}_m|^2/V^2 = \mathcal{F}_m^2/V^2$ because the FT of our spherically symmetric particles is always real. Thus, the average square of the FT from N particles is

$$\langle|\mathcal{F}_t|^2\rangle = \langle\mathcal{F}_t^2\rangle = NV^2\mathcal{S}\cdot\mathcal{P}. \tag{4}$$

Thus, the effective scattering cross section per single particle σ in the PhG can be written in the following form:[34]

$$\sigma = \frac{\omega^4}{16\pi^2c^4}\int_{ESS}\frac{V^2\mathcal{S}(k)\cdot\mathcal{P}(k)}{k_s^2}g(\theta)d^2k, \tag{5}$$

where θ is the angle between scattered $\vec{k}_s$ and input $\vec{k}_{in}$ wavevectors and $g(\theta)$ is a polarization-dependent factor, which for unpolarized light is equal to $(1 + \cos^2\theta)/2$. Here, $\vec{k}$ is the difference between the wave vector of the scattered and incident waves. Besides the dielectric strengths of the individual scatterers, it is the overlap of the Ewald sphere surface (ESS) with the square of the FT in reciprocal space that governs the reflected power. This way, the light scattering can be fully analyzed from the FT of the permittivity.[34] According to the Ewald sphere construction approach [Eq. (5)], for wavelengths becoming shorter, the light–reflection transition from the no-reflection case to the back-reflection case is determined by the sharpness, i.e., the slope of the FT spectrum of $\Delta\varepsilon(\vec{r})$ at the inner boundary of the spherical k-shell. In other words, to achieve a sharp reflection edge, the contributions of the square of the FT of $\Delta\varepsilon(\vec{r})$ inside the shell should be as little as possible, and most importantly, the transition to large values should be sharp.

The form factor in the first-order Born approximation is a constant function in reciprocal space independent of the wavelength of the incident radiation.[34] The first-order Born approximation applied

to a single particle is true only in the Rayleigh–Gans limit where the refractive index contrast of the particle and the phase shift accumulated by light propagating inside the particle are small.[1,3,79]

The first-order Born approximation is a strong tool to describe scattering in disordered structures with a small refractive index contrast in a broad wavelength range. However, it disregards the polarization effects, assuming that all excited access polarizations are parallel to the incident electric field vector. It also assumes weak scatterings such that the incident wave is not depleted and has the same amplitude everywhere. Nonetheless, it can be used to derive the mean free path and the anisotropic scattering factor for ray-tracing simulations or transport equations of systems with multiple scatterings and a strong overall reflection.[85,86,88,89]

If the polarization dependent factor $g(\theta)$ is neglected (scalar approximation), the integral over the Ewald sphere can be simplified to the integral along the radial direction in reciprocal space,

$$\sigma = \frac{\omega^2}{32\pi^3 c^2 n_b^2} \int_0^{2k_{in}} V^2 \mathcal{S}(k) \cdot \mathcal{P}(k) k dk. \tag{6}$$

The functions under the integral in Eq. (6) are all positive, and thus, the integral and the predicted scattering strength in this range monotonically increase with the frequency. The scalar first-order Born approximation cannot predict maxima in scattering efficiency. Still, if the polarization factor $g(\theta)$ is taken into account or only the backward scattering is considered, when only the integration over part of the Ewald sphere is required, then maxima in the reflection spectrum can be expected.

2. Mie scattering

If the Rayleigh–Gans criterion is violated, the single particle should be considered as a resonator. The light propagation through a PhG can be then described mainly by the properties of these resonators calculated by the Mie theory.[1,3] The light incident on the particle can excite magnetic and electric multipoles in the particle that emits scattered waves [Fig. 4(a)]. The scattering cross section Q_{sca} of a spherical particle is given by the electric components a_n and magnetic components b_n,[3]

$$Q_{sca} = \frac{2}{q^2} \sum_{n=1}^{\infty} (2n+1)\left(|a_n|^2 + |b_n|^2\right), \tag{7}$$

$$a_n = \frac{\psi_n'(mq)\psi_n(q) - m\psi_n(mq)\psi_n'(q)}{\psi_n'(mq)\zeta_n(q) - m\psi_n(mq)\zeta_n'(q)}, \tag{8}$$

$$b_n = \frac{m\psi_n'(mq)\psi_n(q) - \psi_n(mq)\psi_n'(q)}{m\psi_n'(mq)\zeta_n(q) - \psi_n(mq)\zeta_n'(q)}, \tag{9}$$

where unitless particle size $q = \frac{\pi d\sqrt{\varepsilon_b}}{\lambda}$, d is the particle diameter, ε_b is the dielectric constant of the background material, ε is the dielectric constant of the particle, $m = \sqrt{\varepsilon/\varepsilon_b}$, and ψ and ζ are Riccati–Bessel functions.[3] In a dilute system, the scattering properties will be defined by single-particle scattering. In a PhG, the particles are touching each other and the interparticle interaction and the short-range order start to play a significant role. The features of Mie resonances are observed in the reflection spectra of

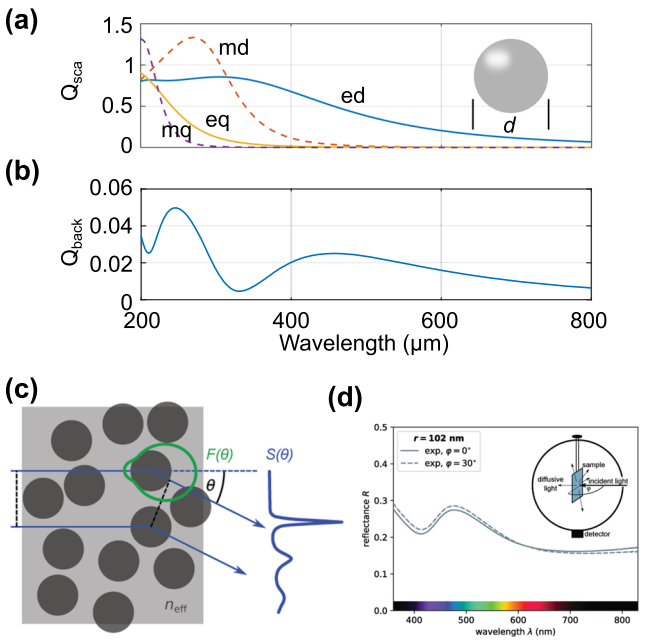

FIG. 4. (a) Calculated scattering cross section (Q_{sca}) from Mie theory and (b) the backscattering cross section (Q_{back}) calculated with the MiePlot software[109] of a spherical particle with a diameter of 172 nm and a refractive index of 1.6. The ed, md, eq, and mq stand for electric and magnetic dipole and electric and magnetic quadrupole contributions to the scattered field, respectively. (c) Scattering defined by the Mie form factor $F(\theta)$ (green) and structure factor $S(\theta)$.[101] (d) Adjusting the effective form factor by the effects from neighboring particles allows fitting the experimental data. Reprinted with permission from Schertel *et al.*, Adv. Opt. Mater. **7**, 1900442 (2019). Copyright 2019 Wiley-VCH.

PhGs.[31,34,39,71,82–84,88] The short-range order can be represented by a combination of the first-order Born approximation with Mie scatters.[81,85,88] In this case, the form factor appearing in the first-order Born approximation is substituted by a term calculated from the Mie theory. The Mie resonances of the single particles are also perturbed by the presence of other particles, which was taken into account in recent publications.[88,101]

The original form factor results from the FT of the motif and it is not changing with the wavelengths of incident radiations. The effective form factor calculated from Mie theory is changing depending on the incident wavenumber k_{in} and direction thus should be written as $F_{k_{in}}(k)$. The $F_{k_{in}}(k)$ contains information about scattering directions of the single particle. The changes in the backscattering of a single particle might result in a significant change in the reflection from PhGs. At the same time, the information about back scatterings is not contained in the total scattering cross section calculations. Thus, the peaks in the reflection from PhG should be better compared with the backscattering efficiency of the single particle [Fig. 4(b)]. For example, it is known that backscattering from a spherical particle can cancel out when magnetic and electric dipole excitations have the same strength.[105–108] This effect can occur at wavelengths away from Mie resonances and can be used to obtain additional selectivity of PhGs.

3. Diffusion theory

If the PhG is thick enough to provide multiple scatterings such that information about the incident direction of the wave is lost, then the light transport can also be described by the diffusion theory.[85–89] The transmission and reflection can be obtained by solving the diffusion equation, which describes photon transport through a diffusing slab of infinite transverse extent. The mean free path l and the directionality of scatterings g define the transport mean free path $l^* = l/(1-g)$. The transmittance $T(\lambda)$ of the light is a function of the transport mean free path and boundary conditions,[85,86,88,110]

$$T(\lambda) = \frac{\ell^*(\lambda) + z_0(\lambda)}{L + 2z_0(\lambda)}, \tag{10}$$

$$z_0(\lambda) = \frac{2}{3}\ell^*(\lambda)\left(\frac{1+R_i}{1-R_i}\right), \tag{11}$$

where L is the thickness of the scattering slab, $z_0(\lambda)$ is an extrapolation length, and R_i is the diffuse reflection coefficient from the film–air interface boundary. The diffuse reflection coefficient is obtained from an angular average of the Fresnel reflection coefficient at the interface.[110,111] For the lossless media, the PhG reflectance $R(\lambda) = 1 - T(\lambda)$.

For the diffusion limit to apply, the thickness of the sample should be much larger than its transport mean free path $L \gg l^*$. For thinner samples with a thickness in the order of the transport mean free path, the approximation might fail and Monte Carlo ray-tracing simulations[87,112] or brute force electromagnetic simulations[34,79] can be required to fit the experimental data. The diffusion theory also takes into account only an angle average reflectivity at the interfaces. However, in thin samples, the scattered light still bears a strong directional anisotropy, and thus, the exact and not the average Fresnel reflection needs to be taken into account to quantify spectral behavior. This will be discussed later.

The effect of neighboring particles on the Mie resonance was estimated by Schertel *et al.*[88] by covering the particle with a shell of background medium so that the particle volume fraction in the core–shell particle corresponds to the particle filling fraction of the PhG. The effective core–shell particle is placed into an effective medium with a refractive index calculated by an energy coherent potential approximation method.[101] In this approximation, the refractive index of the effective medium is chosen in such a way that the average energy density inside the core–shell particle was matched to the energy density inside the medium.[101] This approach approximates the neighboring particles only as an effective medium and disregards the exact effect of coupling between two touching particles. Still, the Mie scattering correction obtained from the constructed core–shell particles provides a better effective form factor [Fig. 4(c)] for the scattering theory and allows fitting experimental data [Fig. 4(d)].

4. Absorption effect

Structural color is a substitution for spectrally selective pigments, but it still requires at least a broadband (black) absorber. As a half-space of scattering medium will sooner or later scatter back all frequency components, an absorber should be used to suppress some of them.

The black absorber can be positioned as a substrate below the PhG layer[32,67] [Fig. 5(a)] or added directly into the PhG structure in small concentrations[32,49,51,67–69] [Fig. 5(b)]. These two options lead to different spectral selectivity. The absorber under the PhG layer absorbs transmitted light and thus differentiates the light by its penetration depth. It is important to achieve the index matching condition between the absorber and PhG such that the transmitted light enters the absorber without significant reflections. The disadvantage of this approach is that the color, in this case, is crucially dependent on the PhG thickness.[32,54,80] A layer that is too thick would lead to a white appearance and a layer that is too thin will appear black. The absorber in the substrate is usually sufficient for blue colors[34,49,57] but is not applicable for long-wavelength color[81] as short wavelengths are stronger scattered [scattering scales with ω^2 in Eq. (6)] and thus have a smaller penetration depth.

On the other hand, the absorber dispersed in the PhG structure selects light by its propagation length. In this case, the half-space PhG approach (infinitely thick layer) can be used to eliminate the thickness dependence. However, the approach is based on the fact that different wavelengths propagate different effective lengths in the PhG structure. For the volume of scattering medium without Fresnel reflection at the boundaries and under diffuse illumination, this is impossible to achieve as the mean propagation length of a photon inside the scattering media is a constant independent of the mean free path and mean transport path[87,112,113] [Fig. 5(c)].

This invariance is valid only without interference between two scattering events (e.g., no photonic bandgaps and localizations). In the weak scattering regime, the photon makes large steps between scattering events and can reflect or transmit through the volume in several steps. In the strong scattering regime, the photon makes short steps between scattering events: many photons are reflected after several scatterings at the surface of the volume, but some of them enter deep into the volume and experience extra-long paths. The average path length stays the same. Since the absorption depends on the photon propagation length, the broadband absorber might not show extra spectral selectivity in this case. Thus, the fact that PhG still shows spectral selectivity in the reflection when the black absorber is added[49,68,69] is not trivial [Figs. 5(a) and 5(b)].

At the same time, absorption is an exponential function of the propagation length, and thus, it depends not only on the average path length but also on the path length distribution, which is still different for different wavelengths.[87] Also, the backscattering from PhGs due to short-range order is an interference effect that might lead to smaller path length and thus less absorption. Still, this selection mechanism is quite weak and leads only to pale colors.[32,35,58,64–67] The higher concentration of the absorber can slightly increase the color purity but significantly decreases the brightness.[49,68,69] The situation might also be different if the excitation is not homogeneous but has a dominant direction, and Fresnel reflection and total internal reflection are taken into account, as discussed in Sec. II C 5.

5. Interface effect

In the light scattering process, the interface between the background material and the PhG slab also plays an important role. In a diffusion approximation, it can be taken into account only via an average reflection coefficient at the boundary. However, this does not constitute a spectrally selective mechanism, as the average reflection has an only weak dependence on wavelength. In the real situation, the total internal reflection can be used to trap

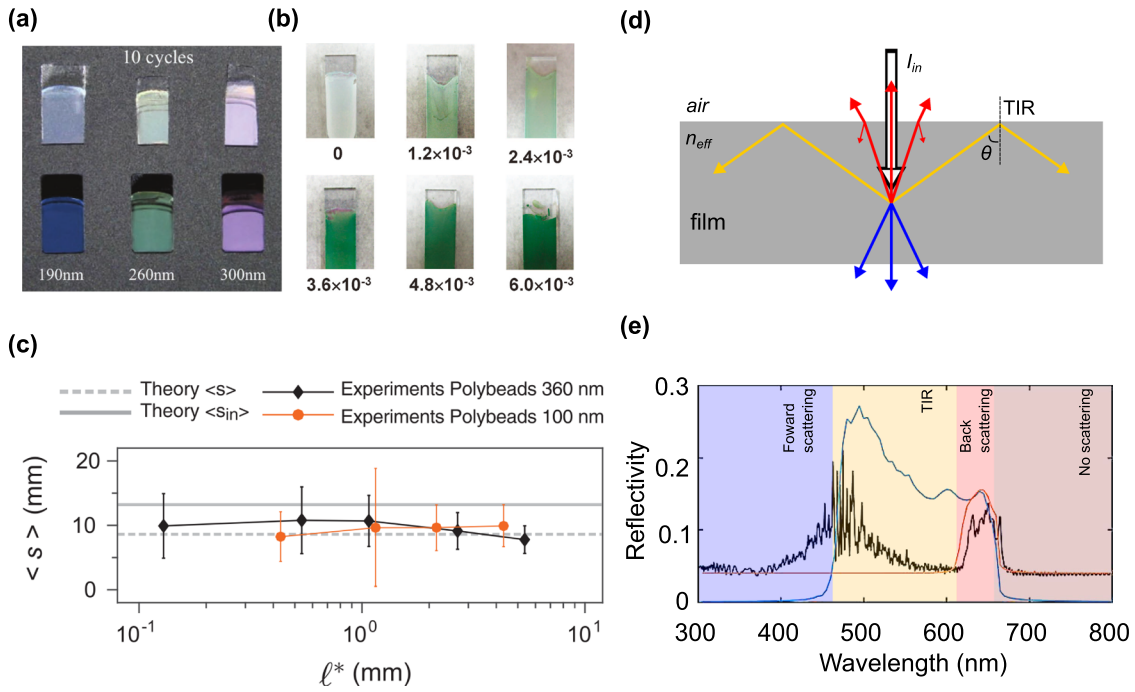

FIG. 5. (a) Broadband absorber put as a substrate beneath the PhG films out of the silica particle size of 190 nm, 260 nm, and 300 nm (lower row) shows better color saturation than the white-substrate samples (upper row). 10 cycles of the layer-by-layer PhG deposition yield a film thickness of about 1.5 μm. Reprinted with permission from Iwata *et al.*, Adv. Mater. **29**, 1605050 (2017). Copyright 2017 Wiley-VCH. (b) The concentration of the absorber embedded in the PhG film influences color purity. The films are out of 260 nm SiO_2 particles on an ITO-coated glass substrate. The amount of carbon black was varied from 0 to 6.0 × 10^{-3} wt. %. Reprinted with permission from Katagiri *et al.*, NPG Asia Mater. **9**, e355 (2017). Copyright 2017 Author(s), licensed under a Creative Commons Attribution 4.0 License. (c) Mean propagation length of light in scattering medium $\langle s \rangle$ is independent of the transport mean free path ℓ^*, which was experimentally verified by the concentration of the polybeads in the scattering medium. Reprinted with permission from Savo *et al.*, Science **358**, 765 (2017). Copyright 2017 AAAS. (d) Internal reflection events of the photons scattered in a disordered medium with a spherical shell in reciprocal space similar to Fig. 3(c). (e) Reflection spectrum simulated from the disordered medium (black) and the prediction from the first-order Born approximation with (orange) and without (blue) Fresnel and TIR reflection.[79]

short-wavelength components and thus obtain red colors, as was proposed for an artificial disordered structure[79] [Figs. 5(d) and 5(e)] and PhGs.[80] In this case, the shorter wavelength components (yellow arrows) are backscattered at larger angles to the normal of the interface between the disordered medium and air and thus will undergo total internal reflection at the interface. It should also be said that the PhG interface to the input medium is intrinsically corrugated, and thus, the total internal reflection condition is always partially circumvented.

The total internal reflection at the interface might also be a main reason for the additional spectral selectivity from adding a broadband absorber to PhGs. The wavelength-dependent scattering angles can lead to trapping of certain wavelength components within a PhG slab, which increases the path lengths for rays of these wavelengths and thus causes a wavelength-dependent absorption, which may enhance selectivity. This mechanism of spectral selectivity is not discussed in detail so far and needs additional considerations.

III. BLUE COLOR

Non-iridescent structural colors produced by PhGs are mostly short-wavelength colors, such as violet or blue (Fig. 6). This is based on the fact that in a long-wavelength limit, PhGs can be considered as a transparent effective medium without scattering. The particle size is then chosen so that the light starts to be scattered at blue and also shorter wavelengths. These scattered wavelengths shorter than those of blue or violet, however, do not contribute to the color impression due to the limited sensitivity of the human eye. The conventional homogeneous particle PhGs show a smooth transition of the reflection edge [Fig. 7(a)] and thus low color purity. This is not significantly improved with the modification of the dielectric strength[27,32,35,51,54] [Figs. 2(c), 3(a), and 6(a)–6(d)]. The packing density is crucial to improve the transition as this directly defines the width of the structure factor peak[34] [Fig. 3(d)]. However, the experimental packing density stays in the 50% range and cannot be significantly changed.[82]

As discussed previously, the selectivity can also be improved by the absorption. The reflection of the longer wavelengths by weak residual scattering by the PhG film can be reduced by broadband absorbers embedded directly into the PhG film.[27,49,57] Higher concentration increases the spectral selectivity of reflection but also reduces the total reflectivity of the sample, thus improving the color purity but at the cost of the lower brightness[49] [Fig. 5(b)].

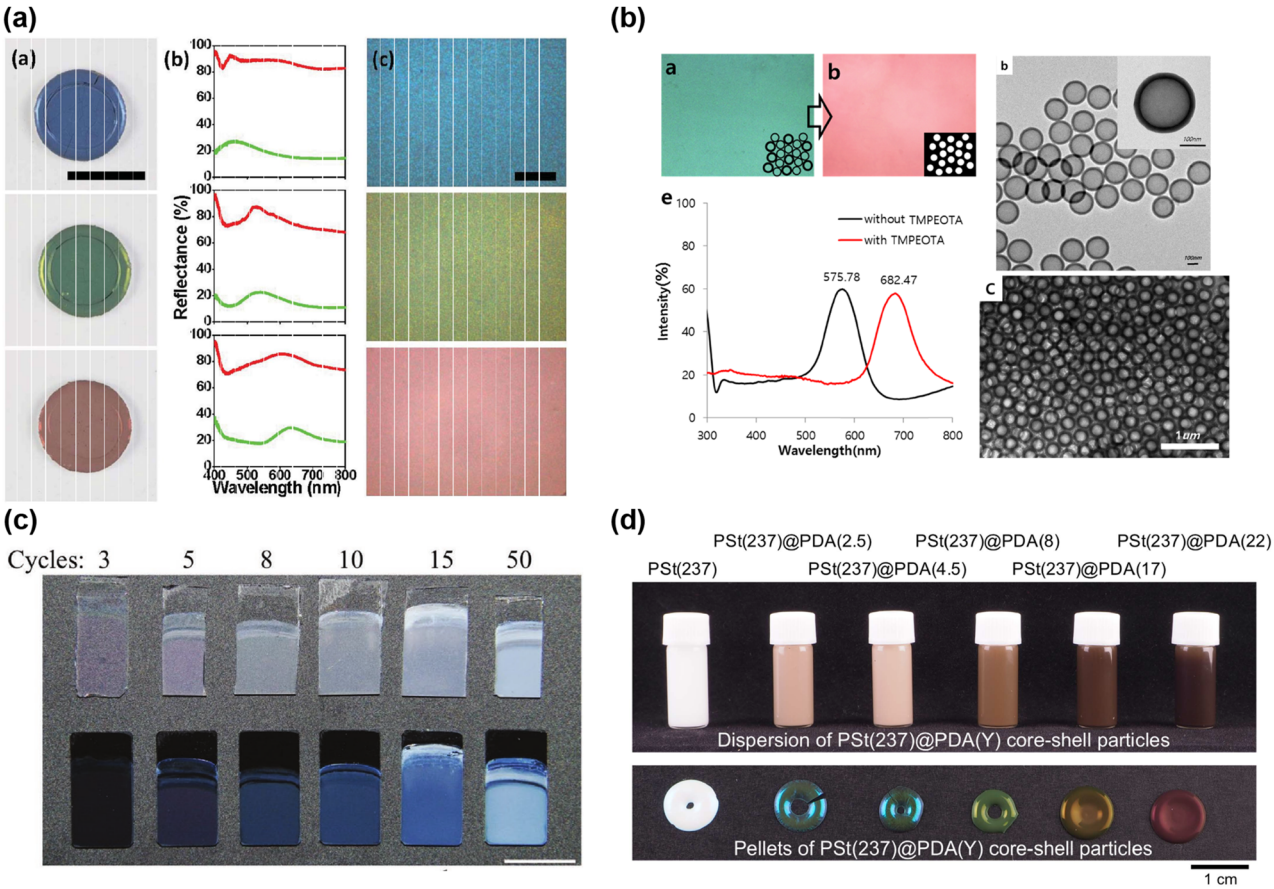

FIG. 6. (a) Color impressions, corresponding reflection spectra, and microscopic optical images of PhGs with PS particle sizes of 200 nm, 240 nm, and 280 nm, respectively. Red and green curves show reflection spectra without or with cuttlefish ink (ink weight ratios of 30%, 33%, and 38% from the top row to bottom row), respectively. Reprinted with permission from Zhang *et al.*, Adv. Mater. **27**, 4719 (2015). Copyright 2015 Wiley-VCH. (b) Color impressions, the spectra, and the microstructure of the PhG made of hollow spheres. Reprinted with permission from Kim *et al.*, ACS Appl. Mater. Interfaces **9**, 24155 (2017). Copyright 2017 American Chemical Society. (c) Color impressions of the PhGs out of 190 nm silica particles and PDDA with different film thicknesses controlled by the deposition cycles of the layer-by-layer method on a clear glass plate and a black quartz plate, respectively. Reprinted with permission from Iwata *et al.*, Adv. Mater. **29**, 1605050 (2017). Copyright 2017 Wiley-VCH. (d) Structural colors of PhGs made of core–shell particles with different shell thicknesses from 0 nm to 22 nm. Reprinted with permission from Kawamura *et al.*, Sci. Rep. **6**, 33984 (2016). Copyright 2016 Author(s), licensed under a Creative Commons Attribution 4.0 License.

Another possibility is the optimization of the PhG motif. In the conventional homogeneous particle based PhGs[32,51] [Figs. 6(a) and 6(b)] and for many core–shell particle based PhGs[39,50,81] [Figs. 6(c) and 6(d)] and in inverted PhGs,[63] the zero point of the form factor is further away from the center of reciprocal space as the structure factor peak.[34] Thus, if at all, it makes the outer side of the peak sharp [Fig. 7(a)]. However, the Ewald sphere starts to touch the structure factor peak from the inner side, probing the relatively shallow slope, intrinsic to the structure factor function. To change that, the zero point of the form factor should be shifted to the inner side of the structure factor peak. In the previous investigations, several examples were presented to achieve such characteristics by employing core–shell particles[34,61] [Figs. 7(b)–7(d)] and surface templated PhGs.[114] The positions in the chromaticity diagram [Fig. 7(e)] calculated from the published reflection spectra are plotted as star (PS full sphere, cuttlefish ink),[35] square (SiO_2 full sphere, carbon black),[49] pentagon (SiO_2 full sphere, carbon black),[32] triangle [PS/poly (NiPAm-AAc) core–shell sphere],[39] circle (PS full sphere, no absorber),[61] hollow circle (YSZ hollow sphere, no absorber),[61] and hollow star (surface templated PhG, no absorber).[114] A significant improvement in color purity was demonstrated with an adjusted motif.

Alternative to motif optimization, a structure factor with vanishing intensity in the sphere of a certain k-radius and a sharp transition to larger wavenumbers can be envisaged. Such structures appear in discussions on hyperuniformity.[115–119] The experimental procedure to pack spherical particles in a 3D hyperuniform configuration is still to be developed.

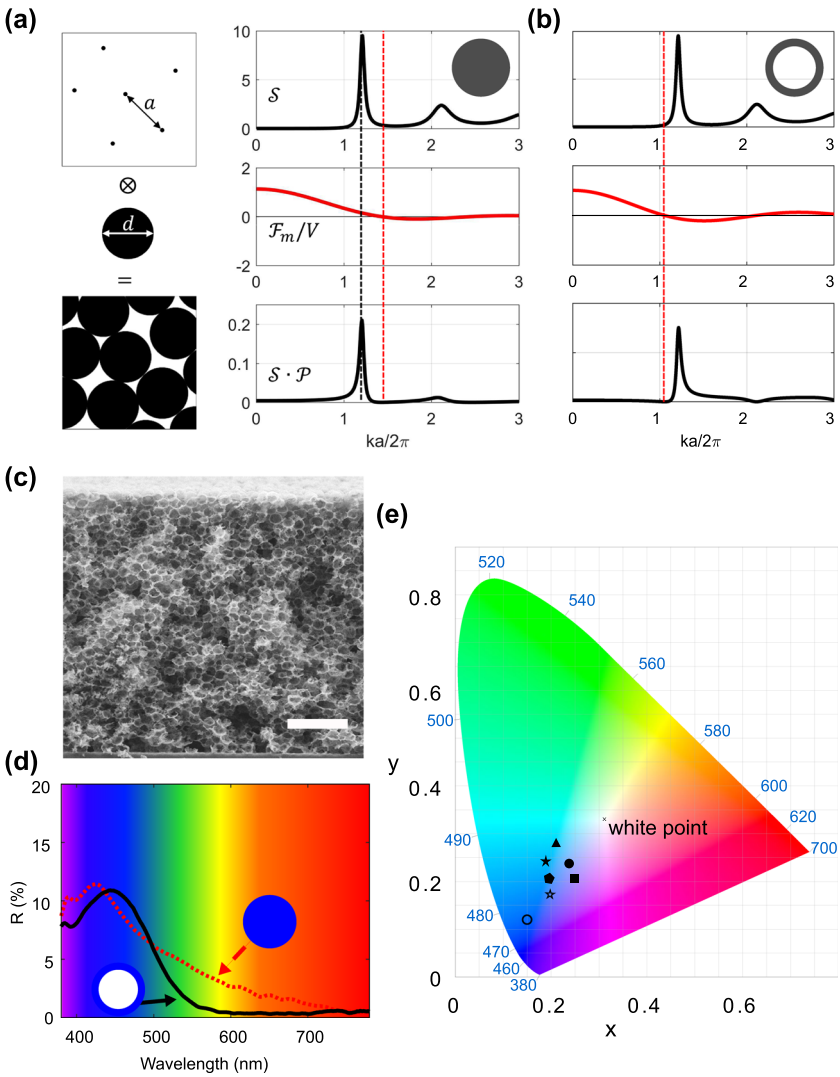

FIG. 7. (a) The real space and reciprocal space representations of the PhG structure out of (a) homogeneous particles and (b) hollow sphere particles. Reprinted with permission from Shang *et al.*, Sci. Rep. **8**, 7804 (2018). Copyright 2018 Author(s), licensed under a Creative Commons Attribution 4.0 License. (c) SEM image of the YSZ hollow sphere PhG. Scale bar is 1 μm. (d) The measured reflection spectrum of a 5.3 μm thick film of a 172 ± 6 nm PS full sphere PhG (red dot curve) and a 5.8 μm thick film of a 316 nm YSZ hollow sphere (shell thickness of 13 nm) PhG (black solid curve), respectively. (e) Optimized hollow sphere based PhG out of yttria stabilized zirconia shows much better color purity, which is indicated by the CIE point (hollow circle) much closer to the perimeter. Reprinted with permission from Shang *et al.*, APL Photonics **4**, 046101 (2019). Copyright 2019 Author(s), licensed under a Creative Commons Attribution 4.0 License.

IV. RED AND OTHER COLORS

To achieve longer wavelength colors such as green or red, a steep reflection edge toward shorter wavelength waves is required [Figs. 2(b) and 2(c)]. This is difficult to obtain as PhG structures always have significant scattering in the short wavelength range, which spoils the long-wavelength color impression[62,79,80] [Fig. 6(a)]. There are different possibilities to explain this short-wavelength scattering in PhG. In a small refractive index contrast regime where the first-order Born approximation applies, the scattering integral for scalar approximation in Eq. (6) is monotonously growing with larger wavenumbers. Thus, shorter wavelengths are always strongly scattered [Fig. 3(c)]. For a large refractive index contrast, the first-order Born approximation is not applicable, but higher-order Mie resonances start to play their role and scatter short-wavelength light.

The peaks in the reflection corresponding to the Mie resonances were used for the green[81,88] and red[35,88] color generation [Fig. 4(d)]. Other colors were also achieved experimentally by increasing either the motif size or the dielectric strength[28,32,38,39,49,50,55,57,63–65,69,72,88] (Fig. 8). Similar to the blue structural color, a broadband absorber[35,64] was introduced to increase color purity [Figs. 8(a)–8(c)]. Schertel *et al.*[88] argued that the absorber concentration solely determines the color purity, while the particle size solely determines the color hue [Fig. 8(d)]. The color purity slightly improves for the optimal absorption length (L_{eff}) at the cost of lower reflected light intensity[49] [Fig. 5(b)]. The broad resonance peak and the overall high scattering efficiency in the whole visible range yield very pale colors.[88] Therefore, introducing and improving the shorter wavelength reflection edge is a key problem for the realization of longer wavelength structural colors.

Magkiriadou *et al.*[81] proposed to use a PhG out of isolated air inclusions to shift the Mie resonances to UV range and to obtain a response in the visible spectrum from the short-range order only.

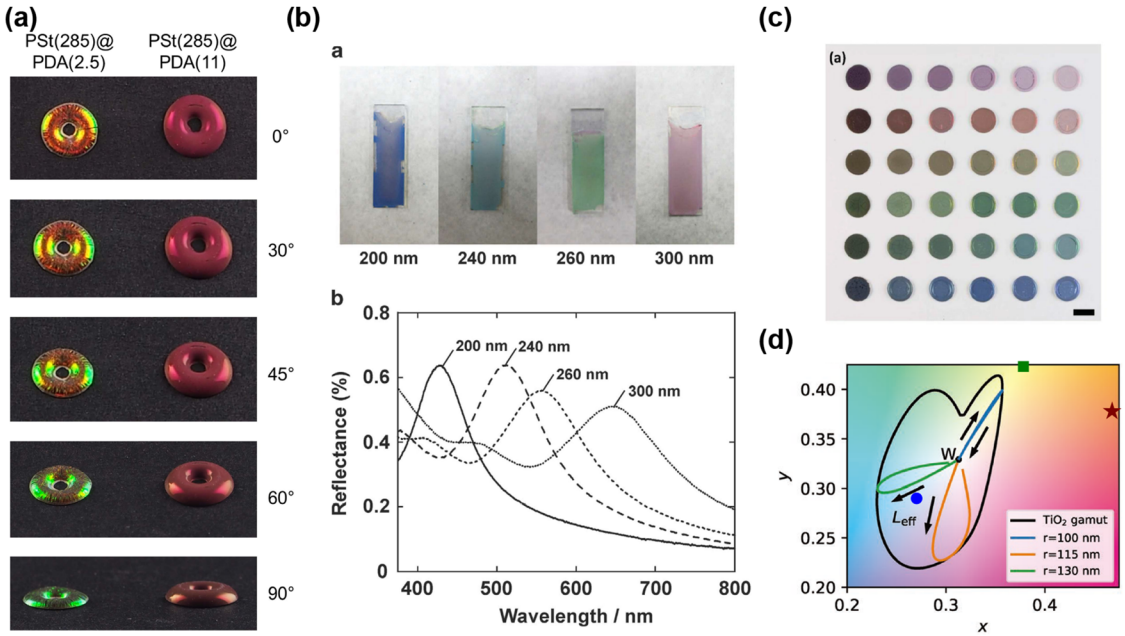

FIG. 8. (a) Structural colors of PhC (left) and PhG (right) made of the core–shell particle structure viewed at different angles. Reprinted with permission from Kawamura *et al.*, Sci. Rep. **6**, 33984 (2016). Copyright 2016 Author(s), licensed under a Creative Commons Attribution 4.0 License. (b) Color impressions and corresponding reflection spectra of PhGs made of homogeneous spherical particles. Reprinted with permission from Katagiri *et al.*, NPG Asia Mater. **9**, e355 (2017). Copyright 2017 Author(s), licensed under a Creative Commons Attribution 4.0 License. (c) Color palette offered by the fabricated PhGs with different particle sizes (increase from bottom to top panels) and black ink particle proportion (decrease from left to right). Reprinted with permission from Zhang *et al.*, Adv. Mater. **27**, 4719 (2015). Copyright 2015 Wiley-VCH. (d) The gamut reachable for polystyrene PhGs (with the radius of 100 nm, 115 nm, and 130 nm) and TiO_2 PhGs, respectively, and the colored loops shows the trajectory with different carbon black concentrations for three different radii. Reprinted with permission from Schertel *et al.*, Adv. Opt. Mater. **7**, 1900442 (2019). Copyright 2019 Wiley-VCH. The CIE points calculated from the reflection spectra in Fig. 6(c) in Ref. 84 are listed as the blue circle (blue), green square (green), and red star (red).

The PhG proposed by Magkiriadou was realized using hollow-core particles[63] [Fig. 6(b)]. In their study, an inverse PhG was achieved by packing hollow spheres and then filling the interstices with a polymer that is index-matched to the sphere shells. The different colors were demonstrated by changing the different average spacing between the air voids by precisely controlling the shell thickness of the hollow spheres. It was shown that the hollow nanospheres produce less short-wavelength scattering than their non-hollow counterparts.[63,84] The CIE points calculated from the reported reflection spectra [Fig. 6(c) in Ref. 84] are presented as the blue circle (blue), green square (green), and red star (red) in Fig. 8(d).

Additionally, the interface can be used to improve color purity, as discussed, via Fresnel reflection and total internal reflection of the short-wavelength components scattered obliquely to the interface.[80] Similar effects were discussed for an artificial disordered structure without Mie resonances and Fresnel reflection to obtain red color.[79] The reflection spectrum from the first-order scattering model shows a sharp reflection transition edge toward the shorter wavelength due to the existence of the total internal reflection of the interfaces.[80] However, the short-wavelength light trapped due to the interface effect can still significantly escape via multiple scatterings.[80] Thus, adjustment of the absorption in the PhG is still required to suppress the totally internally reflected light and further improve the color purity.

V. SUMMARY AND PERSPECTIVES

The color purity is still the key issue for the PhG based structural colors. It was shown that the motif function can be adjusted to significantly improve blue color purity. Core–shell particles with non-monotonous radial refractive index changes are required for that. The blue color can also be further improved by increasing the PhG packing density. This will require modifying the packing methods to the maximum 64% instead of the conventional assembled 50%–55% for PhGs [Fig. 3(d)], which might be addressed by optimization of particle charging or an application of external compression.[82,120]

Highly saturated green and red colors are still key issues. The theoretical and experimental efforts still did not lead to the occurrence of sharp spectral transitions toward small wavelengths. The hollow sphere approach by Magkiridou *et al.*[81] has a promising perspective if Mie resonances are suppressed. However, that also should include careful consideration of total internal reflection at the interface and absorption.[79,80]

Interaction of electric and magnetic response in single particles bears a further perspective to achieve better spectral selectivity, especially for non-blue colors. Adjusting for either forward or backward scattering can be used to enhance spectral selectivity. For that, more complex core–shell particles[106,108] or radially anisotropic particles[105,107] should be considered.

Thus, the perspective of obtaining saturated structural colors lies in the exact adjustment of single-particle responses, short-range order, and absorption and reflection at the interface. It may be possible that even pure red colors can be obtained by proper optimizations.

Another feasible way is the combination of PhG structures and absorbing pigments. Structural color can be used to improve the color purity of a less selective, albeit potentially more stable or less toxic, absorptive pigment. Alternatively, a longer wavelength reflection transition of the PhG can be combined with a shorter wavelength transition of the pigment to generate colors such as green.

The PhG spectral selectivity can be shifted to other spectral ranges and has potential applications beyond structural colors. For example, adjusting the sharp reflection edge to the UV region, the PhG will reflect UV lights and transmit visible lights and thus can be used as a solar UV radiation blocker without the whitening effect. Adjustment of the reflection region to the NIR can help reflect the IR sunlight and still transmit mid-infrared (MIR) thermal radiation for radiative cooling.

ACKNOWLEDGMENTS

This work was funded by the Deutsche Forschungsgemeinschaft (DFG, German Research Foundation) (Grant No. 192346071-SFB 986).

DATA AVAILABILITY

The data that support the findings of this study are available from the corresponding author upon reasonable request.

REFERENCES

[1]M. Born, L. N. L. M. Born, E. Wolf, M. A. X. A. Born, A. B. Bhatia, P. C. Clemmow, D. Gabor, A. R. Stokes, A. M. Taylor, and P. A. Wayman, *Principles of Optics: Electromagnetic Theory of Propagation, Interference and Diffraction of Light* (Cambridge University Press, 1999).
[2]R. W. G. Hunt, *Measuring Colour* (Ellis Horwood Limited, 1991).
[3]C. F. Bohren and D. R. Huffman, *Absorption and Scattering of Light by Small Particles* (Wiley, 2008).
[4]W. Herbst and K. Hunger, *Industrial Organic Pigments: Production, Properties, Applications* (Wiley, 2006).
[5]S. Jo, S. R. Ryu, W. Jang, O.-S. Kwon, B. Rhee, Y. E. Lee, D. Kim, J. Kim, and K. Shin, J. Cult. Heritage **37**, 129–136 (2019).
[6]J. E. Fieberg, P. Knutås, K. Hostettler, and G. D. Smith, Appl. Spectrosc. **71**(5), 794–808 (2017).
[7]M. Jansen and H. P. Letschert, Nature **404**(6781), 980–982 (2000).
[8]K. Mokhtari and S. Salem, RSC Adv. **7**(47), 29899–29908 (2017).
[9]E. Soheyli, S. Behrouzi, Z. Sharifirad, and R. Sahraei, Ceram. Int. **45**(9), 11501–11507 (2019).
[10]T. Zhang, J. Huang, J. Yan, Z. Pu, X. Yin, and Y. Wang, Ceram. Int. **45**(14), 16848–16854 (2019).
[11]L. Ren, H. Lin, F. Meng, and F. Zhang, Ceram. Int. **45**(7), 9646–9652 (2019).
[12]S. Kinoshita and S. Yoshioka, ChemPhysChem **6**(8), 1442–1459 (2005).
[13]A. E. Seago, P. Brady, J.-P. Vigneron, and T. D. Schultz, J. R. Soc., Interface. **6**(suppl 2), S165–S184 (2009).
[14]S. L. Burg and A. J. Parnell, J. Phys.: Condens. Matter **30**(41), 413001 (2018).
[15]V. E. Johansen, L. Catón, R. Hamidjaja, E. Oosterink, B. D. Wilts, T. S. Rasmussen, M. M. Sherlock, C. J. Ingham, and S. Vignolini, Proc. Natl. Acad. Sci. U. S. A. **115**(11), 2652–2657 (2018).
[16]M. Song, D. Wang, S. Peana, S. Choudhury, P. Nyga, Z. A. Kudyshev, H. Yu, A. Boltasseva, V. M. Shalaev, and A. V. Kildishev, Appl. Phys. Rev. **6**(4), 041308 (2019).
[17]C.-S. Park, I. Koirala, S. Gao, V. R. Shrestha, S.-S. Lee, and D.-Y. Choi, Opt. Express **27**(2), 667–679 (2019).
[18]K. T. Lee, S. Y. Han, Z. Li, H. W. Baac, and H. J. Park, Sci. Rep. **9**(1), 14917 (2019).
[19]L. Cheng, K. Wang, J. Mao, X. M. Goh, Z. Chu, Y. Zhang, and L. Zhang, Ann. Phys. **531**(9), 1900073 (2019).
[20]G. Shang, P. Dyachenko, E. W. Leib, T. Vossmeyer, A. Petrov, and M. Eich, Ceram. Int. **46**(11PB), 19241–19247 (2020).
[21]S.-H. Kim, S. Y. Lee, S.-M. Yang, and G.-R. Yi, NPG Asia Mater. **3**(1), 25–33 (2011).
[22]G. L. Shang, Y. Zhang, G. T. Fei, Y. Su, and L. D. Zhang, Ann. Phys. **528**(3-4), 288–294 (2016).
[23]X. Wang, Z. Wang, L. Bai, H. Wang, L. Kang, D. H. Werner, M. Xu, B. Li, J. Li, and X.-F. Yu, Opt. Express **26**(21), 27001–27013 (2018).
[24]M. Umar, K. Min, and S. Kim, APL Photonics **4**(12), 120901 (2019).
[25]S. Kinoshita, S. Yoshioka, and J. Miyazaki, Rep. Prog. Phys. **71**(7), 076401 (2008).
[26]C. I. Aguirre, E. Reguera, and A. Stein, ACS Appl. Mater. Interfaces **2**(11), 3257–3262 (2010).
[27]Y. Takeoka, J. Mater. Chem. **22**(44), 23299–23309 (2012).
[28]N. Vogel, S. Utech, G. T. England, T. Shirman, K. R. Phillips, N. Koay, I. B. Burgess, M. Kolle, D. A. Weitz, and J. Aizenberg, Proc. Natl. Acad. Sci. U. S. A. **112**(35), 10845–10850 (2015).
[29]D. T. Meiers, M. C. Heep, and G. von Freymann, APL Photonics **3**(10), 100802 (2018).
[30]J. Ballato, J. Dimaio, A. James, and E. Gulliver, Appl. Phys. Lett. **75**(11), 1497–1499 (1999).
[31]P. D. García, R. Sapienza, Á. Blanco, and C. López, Adv. Mater. **19**(18), 2597 (2007).
[32]M. Iwata, M. Teshima, T. Seki, S. Yoshioka, and Y. Takeoka, Adv. Mater. **29**(26), 1605050 (2017).
[33]H. Noh, S. F. Liew, V. Saranathan, S. G. Mochrie, R. O. Prum, E. R. Dufresne, and H. Cao, Adv. Mater. **22**(26-27), 2871–2880 (2010).
[34]G. Shang, L. Maiwald, H. Renner, D. Jalas, M. Dosta, S. Heinrich, A. Petrov, and M. Eich, Sci. Rep. **8**(1), 7804 (2018).
[35]Y. Zhang, B. Dong, A. Chen, X. Liu, L. Shi, and J. Zi, Adv. Mater. **27**(32), 4719–4724 (2015).
[36]D. P. Josephson, M. Miller, and A. Stein, Z. Anorg. Allg. Chem. **640**(3-4), 655–662 (2014).
[37]M. Xiao, Z. Hu, Z. Wang, Y. Li, A. D. Tormo, N. Le Thomas, B. Wang, N. C. Gianneschi, M. D. Shawkey, and A. Dhinojwala, Sci. Adv. **3**(9), e1701151 (2017).
[38]H. C. Gu, B. F. Ye, H. B. Ding, C. H. Liu, Y. J. Zhao, and Z. Z. Gu, J. Mater. Chem. C **3**(26), 6607–6612 (2015).
[39]J.-G. Park, S.-H. Kim, S. Magkiriadou, T. M. Choi, Y.-S. Kim, and V. N. Manoharan, Angew. Chem., Int. Ed. Engl. **53**(11), 2899–2903 (2014).
[40]K.-T. Lee, C. G. Ji, D. Banerjee, and L. J. Guo, Laser Photonics Rev. **9**(3), 354–362 (2015).
[41]A. Kristensen, J. K. W. Yang, S. I. Bozhevolnyi, S. Link, P. Nordlander, N. J. Halas, and N. A. Mortensen, Nat. Rev. Mater. **2**(1), 16088 (2016).
[42]H. Liu, W. Lin, and M. Hong, APL Photonics **4**(5), 051101 (2019).
[43]K. Wilson, C. A. Marocico, and A. L. Bradley, J. Phys. D: Appl. Phys. **51**(25), 255101 (2018).
[44]T. Sai, B. D. Wilts, A. Sicher, U. Steiner, F. Scheffold, and E. R. Dufresne, CHIMIA Int. J. Chem. **73**(1), 47–50 (2019).

[45]R. N. K. Taylor, F. Seifrt, O. Zhuromskyy, U. Peschel, G. Leugering, and W. Peukert, Adv. Mater. **23**(22-23), 2554–2570 (2011).
[46]S. Torquato and F. H. Stillinger, Rev. Mod. Phys. **82**(3), 2633–2672 (2010).
[47]J. A. Barker and D. Henderson, Rev. Mod. Phys. **48**(4), 587–671 (1976).
[48]S. Torquato, T. M. Truskett, and P. G. Debenedetti, Phys. Rev. Lett. **84**(10), 2064–2067 (2000).
[49]K. Katagiri, Y. Tanaka, K. Uemura, K. Inumaru, T. Seki, and Y. Takeoka, NPG Asia Mater. **9**(3), e355 (2017).
[50]P. Liu, J. Chen, Z. Zhang, Z. Xie, X. Du, and Z. Gu, Nanoscale **10**(8), 3673–3679 (2018).
[51]J. D. Forster, H. Noh, S. F. Liew, V. Saranathan, C. F. Schreck, L. Yang, J. G. Park, R. O. Prum, S. G. Mochrie, C. S. O'Hern, H. Cao, and E. R. Dufresne, Adv. Mater. **22**(26-27), 2939–2944 (2010).
[52]F. Meng, M. M. Umair, K. Iqbal, X. Jin, S. Zhang, and B. Tang, ACS Appl. Mater. Interfaces **11**(13), 13022–13028 (2019).
[53]V. Saranathan, J. D. Forster, H. Noh, S.-F. Liew, S. G. Mochrie, H. Cao, E. R. Dufresne, and R. O. Prum, J. R. Soc. Interface. **9**(75), 2563–2580 (2012).
[54]Y. Häntsch, G. Shang, A. Petrov, M. Eich, and G. A. Schneider, Adv. Opt. Mater. **7**(18), 1900428 (2019).
[55]L. Bai, V. C. Mai, Y. Lim, S. Hou, H. Mohwald, and H. Duan, Adv. Mater. **30**(9), 1705667 (2018).
[56]A. G. Dumanli and T. Savin, Chem. Soc. Rev. **45**(24), 6698–6724 (2016).
[57]A. Kawamura, M. Kohri, G. Morimoto, Y. Nannichi, T. Taniguchi, and K. Kishikawa, Sci. Rep. **6**, 33984 (2016).
[58]M. Kohri, Y. Nannichi, T. Taniguchi, and K. Kishikawa, J. Mater. Chem. C **3**(4), 720–724 (2015).
[59]Y. X. Zhang, P. Han, H. Y. Zhou, N. Wu, Y. Wei, X. Yao, J. M. Zhou, and Y. L. Song, Adv. Funct. Mater. **28**(29), 1802585 (2018).
[60]Z. Zhu, J. Zhang, Y.-l. Tong, G. Peng, T. Cui, C.-F. Wang, S. Chen, and D. A. Weitz, ACS Photonics **6**(1), 116–122 (2019).
[61]G. Shang, Y. Häntsch, K. P. Furlan, R. Janssen, G. A. Schneider, A. Petrov, and M. Eich, APL Photonics **4**(4), 046101 (2019).
[62]S. Magkiriadou, J.-G. Park, Y.-S. Kim, and V. N. Manoharan, Opt. Mater. Express **2**(10), 1343–1352 (2012).
[63]S.-H. Kim, S. Magkiriadou, D. K. Rhee, D. S. Lee, P. J. Yoo, V. N. Manoharan, and G.-R. Yi, ACS Appl. Mater. Interfaces **9**(28), 24155–24160 (2017).
[64]Y. Cui, F. Wang, J. Zhu, W. Wu, Y. Qin, and X. Zhang, J. Colloid Interface Sci. **531**, 609–617 (2018).
[65]T. Iwasaki, Y. Tamai, M. Yamamoto, T. Taniguchi, K. Kishikawa, and M. Kohri, Langmuir **34**(39), 11814–11821 (2018).
[66]M. Xiao, Y. Li, M. C. Allen, D. D. Deheyn, X. Yue, J. Zhao, N. C. Gianneschi, M. D. Shawkey, and A. Dhinojwala, ACS Nano **9**(5), 5454–5460 (2015).
[67]X. Yang, D. Ge, G. Wu, Z. Liao, and S. Yang, ACS Appl. Mater. Interfaces **8**(25), 16289–16295 (2016).
[68]A. Kawamura, M. Kohri, S. Yoshioka, T. Taniguchi, and K. Kishikawa, Langmuir **33**(15), 3824–3830 (2017).
[69]Y. Takeoka, S. Yoshioka, A. Takano, S. Arai, K. Nueangnoraj, H. Nishihara, M. Teshima, Y. Ohtsuka, and T. Seki, Angew. Chem., Int. Ed. Engl. **52**(28), 7261–7265 (2013).
[70]Q. Li, Y. Zhang, L. Shi, H. Qiu, S. Zhang, N. Qi, J. Hu, W. Yuan, X. Zhang, and K.-Q. Zhang, ACS Nano **12**(4), 3095–3102 (2018).
[71]S. G. Romanov, S. Orlov, D. Ploss, C. K. Weiss, N. Vogel, and U. Peschel, Sci. Rep. **6**, 27264 (2016).
[72]D. Ge, E. Lee, L. Yang, Y. Cho, M. Li, D. S. Gianola, and S. Yang, Adv. Mater. **27**(15), 2489–2495 (2015).
[73]T. Kuno, Y. Matsumura, K. Nakabayashi, and M. Atobe, Angew. Chem., Int. Ed. Engl. **55**(7), 2503–2506 (2016).
[74]I. Lee, D. Kim, J. Kal, H. Baek, D. Kwak, D. Go, E. Kim, C. Kang, J. Chung, Y. Jang, S. Ji, J. Joo, and Y. Kang, Adv. Mater. **22**(44), 4973–4977 (2010).
[75]Y. Luo, J. Zhang, A. Sun, C. Chu, S. Zhou, J. Guo, T. Chen, and G. Xu, J. Mater. Chem. C **2**(11), 1990 (2014).
[76]J. F. Zhang, C. Y. Chu, A. H. Sun, S. Ma, X. X. Qiao, C. Y. Wang, J. J. Guo, Z. X. Li, and G. J. Xu, J. Alloys Compd. **654**, 251–256 (2016).
[77]S. Mohd-Noor, H. Jang, K. Baek, Y.-R. Pei, A.-M. Alam, Y. H. Kim, I. S. Kim, J.-H. Choy, and J. K. Hyun, J. Mater. Chem. A **7**(17), 10561–10571 (2019).
[78]C. W. Hsu, O. D. Miller, S. G. Johnson, and M. Soljačić, Opt. Express **23**(7), 9516–9526 (2015).
[79]L. Maiwald, S. Lang, D. Jalas, H. Renner, A. Y. Petrov, and M. Eich, Opt. Express **26**(9), 11352–11365 (2018).
[80]V. Hwang, A. B. Stephenson, S. Magkiriadou, J. G. Park, and V. N. Manoharan, Phys. Rev. E **101**(1-1), 012614 (2020).
[81]S. Magkiriadou, J. G. Park, Y. S. Kim, and V. N. Manoharan, Phys. Rev. E **90**(6), 062302 (2014).
[82]P. D. Garcia, R. Sapienza, J. Bertolotti, M. D. Martin, A. Blanco, A. Altube, L. Vina, D. S. Wiersma, and C. Lopez, Phys. Rev. A **78**(2), 023823 (2008).
[83]M. Retsch, M. Schmelzeisen, H.-J. Butt, and E. L. Thomas, Nano Lett. **11**(3), 1389–1394 (2011).
[84]S. H. Kim, V. Hwang, S. G. Lee, J. W. Ha, V. N. Manoharan, and G. R. Yi, Small **15**(23), e1900931 (2019).
[85]P. D. Kaplan, A. D. Dinsmore, A. G. Yodh, and D. J. Pine, Phys. Rev. E **50**(6), 4827–4835 (1994).
[86]L. F. Rojas-Ochoa, J. M. Mendez-Alcaraz, J. J. Saenz, P. Schurtenberger, and F. Scheffold, Phys. Rev. Lett. **93**(7), 073903 (2004).
[87]R. Savo, R. Pierrat, U. Najar, R. Carminati, S. Rotter, and S. Gigan, Science **358**(6364), 765–768 (2017).
[88]L. Schertel, L. Siedentop, J. M. Meijer, P. Keim, C. M. Aegerter, G. J. Aubry, and G. Maret, Adv. Opt. Mater. **7**(15), 1900442 (2019).
[89]S. Fraden and G. Maret, Phys. Rev. Lett. **65**(4), 512–515 (1990).
[90]B. Q. Dong, X. H. Liu, T. R. Zhan, L. P. Jiang, H. W. Yin, F. Liu, and J. Zi, Opt. Express **18**(14), 14430–14438 (2010).
[91]J. Ballato, J. Opt. Soc. Am. B **17**(2), 219 (2000).
[92]G. D. Scott and D. M. Kilgour, J. Phys. D: Appl. Phys. **2**(6), 863–866 (1969).
[93]T. Li, A. J. Senesi, and B. Lee, Chem. Rev. **116**(18), 11128–11180 (2016).
[94]J. K. Percus and G. J. Yevick, Phys. Rev. **110**(1), 1–13 (1958).
[95]D. Frenkel, R. J. Vos, C. G. de Kruif, and A. Vrij, J. Chem. Phys. **84**(8), 4625–4630 (1986).
[96]F. Scheffold and T. G. Mason, J. Phys.: Condens. Matter **21**(33), 332102 (2009).
[97]J. F. Galisteo-López, M. Ibisate, R. Sapienza, L. S. Froufe-Pérez, Á. Blanco, and C. López, Adv. Mater. **23**(1), 30–69 (2011).
[98]Z. Y. Cai, J. H. Teng, Q. F. Yan, and X. S. Zhao, Colloids Surf., A **402**, 37–44 (2012).
[99]Q. Yan, L. Gao, V. Sharma, Y.-M. Chiang, and C. C. Wong, Langmuir **24**(20), 11518–11522 (2008).
[100]A. Emoto and T. Fukuda, Appl. Phys. Lett. **100**(13), 131901 (2012).
[101]G. J. Aubry, L. Schertel, M. D. Chen, H. Weyer, C. M. Aegerter, S. Polarz, H. Colfen, and G. Maret, Phys. Rev. A **96**(4), 043871 (2017).
[102]A. I. Kuznetsov, A. E. Miroshnichenko, Y. H. Fu, J. Zhang, and B. Luk'yanchuk, Sci. Rep. **2**, 492 (2012).
[103]C. Rockstuhl and F. Lederer, Phys. Rev. B **79**(13), 132202 (2009).
[104]G. Shang, K. P. Furlan, R. Zierold, R. H. Blick, R. Janssen, A. Petrov, and M. Eich, Sci. Rep. **9**(1), 11379 (2019).
[105]H. Chew and M. Kerker, J. Opt. Soc. Am. **66**(5), 445–449 (1976).
[106]Z. Ruan and S. Fan, Phys. Rev. Lett. **105**(1), 013901 (2010).
[107]A. I. Kuznetsov, A. E. Miroshnichenko, M. L. Brongersma, Y. S. Kivshar, and B. Luk'yanchuk, Science **354**(6314), aag2472 (2016).
[108]W. Liu, J. Zhang, B. Lei, H. Ma, W. Xie, and H. Hu, Opt. Express **22**(13), 16178–16187 (2014).
[109]See http://www.philiplaven.com/mieplot.htm for MiePlot, 2018.
[110]N. Garcia, A. Z. Genack, and A. A. Lisyansky, Phys. Rev. B **46**(22), 14475–14479 (1992).
[111]J. X. Zhu, D. J. Pine, and D. A. Weitz, Phys. Rev. A **44**(6), 3948–3959 (1991).
[112]A. Mazzolo, C. de Mulatier, and A. Zoia, J. Math. Phys. **55**(8), 083308 (2014).
[113]R. Pierrat, P. Ambichl, S. Gigan, A. Haber, R. Carminati, and S. Rotter, Proc. Natl. Acad. Sci. U. S. A. **111**(50), 17765–17770 (2014).
[114]G. Shang, K. P. Furlan, R. Janssen, A. Petrov, and M. Eich, Opt. Express **28**(6), 7759–7770 (2020).

[115]G. Gkantzounis, T. Amoah, and M. Florescu, Phys. Rev. B **95**(9), 094120 (2017).
[116]W. Man, M. Florescu, K. Matsuyama, P. Yadak, G. Nahal, S. Hashemizad, E. Williamson, P. Steinhardt, S. Torquato, and P. Chaikin, Opt. Express **21**(17), 19972–19981 (2013).
[117]S. Torquato, J. Phys.: Condens. Matter **28**(41), 414012 (2016).
[118]C. E. Zachary, Y. Jiao, and S. Torquato, Phys. Rev. Lett. **106**(17), 178001 (2011).
[119]M. Castro-Lopez, M. Gaio, S. Sellers, G. Gkantzounis, M. Florescu, and R. Sapienza, APL Photonics **2**(6), 061302 (2017).
[120]D. Montesdeoca, F. Bayat, A. Espinha, Á. Blanco, C. Pecharromán, and C. López, Part. Part. Syst. Charact. **33**(12), 871–877 (2016).